

Sub-optical-cycle manipulation of valley-polarized currents

Wenqing Li¹, Xiaosong Zhu^{1,3*}, Liang Li¹, Wanzhu He¹, Jie Long¹,
Pengfei Lan^{1,3†}, Peixiang Lu^{1,2,3‡}

¹Wuhan National Laboratory for Optoelectronics and School of Physics, Huazhong University of Science and Technology, Wuhan 430074, China.

²Hubei Key Laboratory of Optical Information and Pattern Recognition,
Wuhan Institute of Technology, Wuhan 430205, China.

³Hubei Optical Fundamental Research Center, Wuhan 430074, China.

*Corresponding author. Email: zhuxiaosong@hust.edu.cn

†Corresponding author. Email: pengfeilan@hust.edu.cn

‡Corresponding author. Email: lupeixiang@hust.edu.cn

Manipulating valley-polarized currents at optical frequencies is the key to petahertz valleytronics, yet it remains intractable. To tackle this challenge, we propose an all-optical scheme using non-resonant bichromatic optical fields, which allow for the control of sub-cycle electron dynamics. The combined effect of the helical and asymmetric waveforms of the optical fields leads to the valley-polarization and displacement of the excited electrons concurrently, thereby inducing the valley-polarized currents, on the sub-optical-cycle timescale. This scheme inherently possesses remarkable resilience to decoherence, making it particularly suitable for materials with short decoherence times. Moreover, the direction of the currents can be precisely controlled by adjusting the relative phase of the bichromatic

components. Our scheme offers a promising avenue for generating and modulating valley-polarized currents at the femtosecond timescale, opening the door to the realm of petahertz valleytronics.

1 Introduction

In the electronic band structure of a material, local minima in the conduction band (CB) or local maxima in the valence band (VB) are referred to as valleys. When the electrons are excited across the band gap from the highest VB into these minima in the first CB, they may share the same energy but possess different crystal momenta. Thus, the electrons in these materials exhibit valley degrees of freedom in addition to charge and spin. The valley degree of freedom holds promise for energy-efficient information storage and presents intriguing prospects for going beyond classical information processing (1–3).

Utilizing the opposite Berry curvature associated with the different valleys, precisely addressing these valleys has been achieved in diverse materials (4–15). Since the valley index is a concept within the reciprocal space, the next pivotal challenge in valleytronic devices is how to transfer the valley-polarized information to the external environment (3). One promising solution is to generate and deliver the valley-polarized currents (with or without net charge current). Over the past two decades, numerous efforts have been devoted to generating valley-polarized currents (16–25), including designing valley filters (16) and valleytronic transistor (17), utilizing the valley-Hall effect (18–20) and employing advanced strain engineering techniques (22–25), etc. These approaches rely on rigid architectures, such as a fixed pair of electrodes to supply a strong external bias or organized heterostructures (21). It is also proposed to generate valley-polarized currents utilizing strong terahertz (THz) pulses (26, 27), whose periods in experiments are typically on the picosecond scale. Despite all the above advances, the inherent characteristics of these configurations have precluded access to femtosecond dynamics and possible applications at petahertz (PHz) rates.

To advance into the PHz regime, an all-optical approach is essentially required, where the applied fields oscillate at optical frequencies with femtosecond scale periods. To address this critical void, in this work, we introduce an all-optical scheme to generate and modulate valley-polarized currents. It is realized by engineering the sub-cycle electron dynamics with non-resonant

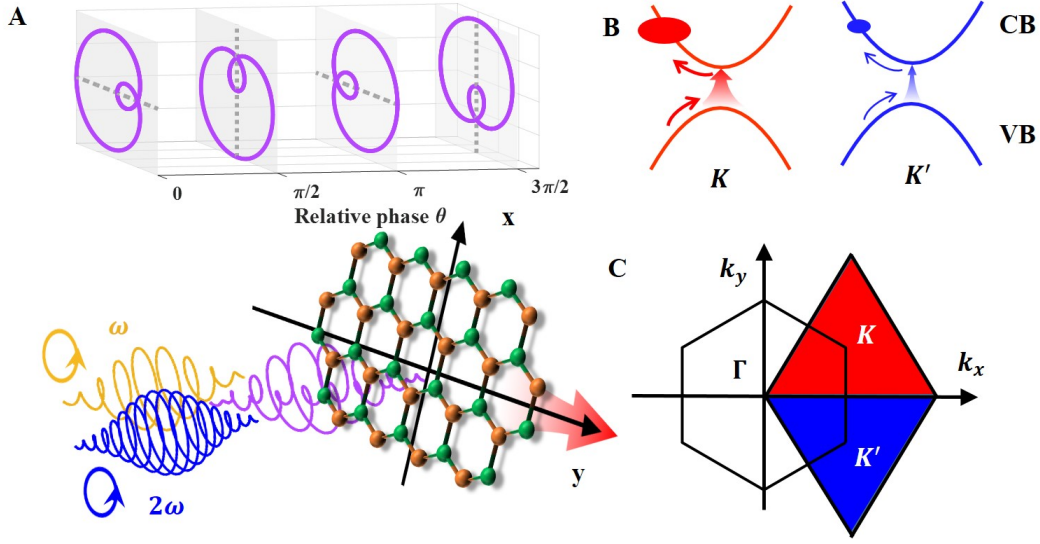


Fig. 1: (A) The main panel schematically illustrates the manipulation of valley-polarized currents in 2D materials driven by the co-rotating bicircular field. The upper panel shows the Lissajous figures of the co-rotating bicircular fields with different relative phases. (B) The schematic illustration of the excited electrons in the VB and CB around two valleys. (C) The first Brillouin zone (BZ) is separated into two regions around two valleys, as indicated by the red and blue regions.

tailored nontrivial optical fields (28–38) that consist of a circularly-polarized fundamental field and its co-rotating second harmonic. The combined effect of the helical and asymmetric waveforms of the fields leads to the valley-polarization and displacement of the excited electrons concurrently, giving rise to valley-polarized currents, on the sub-optical-cycle timescale. The feasibility of the scheme is demonstrated by numerical simulations for the two typical categories of valley-active materials, gapped graphene and transition metal dichalcogenides (TMDs), based on a tight-binding model and the time-dependent density functional theory (TDDFT), respectively. Moreover, the particular mechanism ensures that this scheme is robust against decoherence. Numerical results show that the purity of the valley-polarized currents can be only slightly degenerated by less than one-twelfth even when the decoherence time is reduced to 5 femtoseconds. Besides, it is also shown that the direction of the currents can be precisely controlled by adjusting the relative phase of the bichromatic components. Our approach represents a promising strategy for manipulating high-purity valley-polarized currents at the femtosecond timescale and paves a path toward the realization of PHz valleytronic devices.

Results

Valley-polarized current manipulation via tailored optical fields

Here, we outline the basic concept and offer guidelines for designing the tailored optical driving fields aimed at generating valley-polarized currents. To obtain valley-polarized currents, two conditions are required: electron excitation predominantly takes place in one valley over the other, and the excited electrons are asymmetrically distributed around the valley. Thus, the driving field must concurrently satisfy two crucial criteria. It should induce different electron dynamics in respective valleys and it must be capable of provoking the displacement of excited electrons. In this context, a co-rotating bicircular field, composed of a circularly polarized fundamental-frequency field and a frequency-doubling field with the same helicity, will fulfill the aforementioned requirements. Its helical waveform drives distinct electron dynamics around different valleys with opposite Berry curvature. Simultaneously, its asymmetric waveform displaces the excited population inducing the valley-polarized currents. Considering the co-rotating driving laser is polarized in the $x - y$ plane and traveling in the z -direction as illustrated in the main panel in Fig. 1A, its electric field can be described by:

$$\mathbf{F}_{\text{co}}(t) = \frac{1}{\sqrt{2}} \begin{bmatrix} F_1 \cos(\omega t) + F_2 \cos(2\omega t + \theta) \\ F_1 \sin(\omega t) + F_2 \sin(2\omega t + \theta) \end{bmatrix}. \quad (1)$$

ω is the frequency of the fundamental component. F_1 and F_2 are the amplitudes of each circularly-polarized component, corresponding to intensity I_1 and I_2 , respectively. θ is the relative phase between the bichromatic components. Recent developments in modern light generation technology have enabled the customization of nontrivial optical waveforms by synthesizing lights with different colors (29, 30, 39–41), and thus such a field is readily available in experiments.

For simplicity, we consider $F_1 = F_2 = F_0$. Equation 1 can be factorized and rewritten as $\mathbf{F}_{\text{co}}(t) = \sqrt{2}F_0 \cos(\frac{\omega t + \theta}{2}) [\cos(\frac{3\omega t + \theta}{2}), \sin(\frac{3\omega t + \theta}{2})]^\top$, which indicates that the $\omega - 2\omega$ co-rotating driving field can be viewed as a circularly-polarized field modulated by $\cos(\frac{\omega t + \theta}{2})$ (35, 42). Then, one can obtain

$$F_{\text{co}}^2(t) = 2F_0^2 \cos^2(\frac{\omega t + \theta}{2}) = F_0^2(1 + \cos(\omega t + \theta)). \quad (2)$$

Namely, the magnitude of the field $F_{\text{co}}^2(t)$ exhibits a cos-type modulation around 1, which indicates that the waveform of co-rotating bicircular fields (including not only the electric field but also

the vector potential $\mathbf{A}(t) = -\int_{-\infty}^t \mathbf{F}(t')dt'$ is naturally asymmetric. The electric field reaches the maximum value at $\omega t = -\theta + 2\pi N$ (N is an integer). Therefore, the symmetric axis of the corresponding Lissajous figure, which aligns with the maximum and minimum values of F_{co}^2 , as indicated by the dashed grey lines in the upper panel in Fig. 1A, is oriented along $\mathbf{e}_\phi = \cos(-\theta)\mathbf{e}_x + \sin(-\theta)\mathbf{e}_y$. Here, \mathbf{e}_x (\mathbf{e}_y) represents the unit vector along the x (y)-direction. \mathbf{e}_ϕ represents another unit vector, which makes an angle ϕ with \mathbf{e}_x . Here, $\phi = -\theta$. Therefore, the orientation of the waveform can be controlled by θ , as illustrated in the upper panel in Fig. 1A.

As shown in Fig. 1B, once the co-rotating bicircular field illuminates the 2D hexagonal materials lying in the $x - y$ plane, the electrons are pre-accelerated in the VB before being excited to the CB in the vicinity of the valleys (43, 44). The excitation predominately occurs when the electric field reaches its maximum of each optical cycle (e.g. see Fig. 2B). After the excitation, the electrons continue to evolve in the CB with the driving field, occupying different regions in the BZ. The electron wavepacket evolves in the reciprocal space according to the Bloch acceleration theorem ($\mathbf{k}(t) = \mathbf{k}_{\text{ex}} + \mathbf{A}(t)$, \mathbf{k}_{ex} is the electron wavenumber of the excited electron). Therefore, the vector potential $\mathbf{A}(t)$ is the quantity responsible for the asymmetric electron population symmetry in each valley (see Fig. 1B), and the excited population is displaced along the negative direction of the maximum of $\mathbf{A}(t)$. Consequently, the nonlinear residual photocurrents along the negative direction of the maximum of $\mathbf{A}(t)$ are obtained (for a particular example, see Fig. 2). Meanwhile, due to the helical waveform of the field synthesized by the two co-rotating components, the electrons around one valley can be dominantly excited, as indicated by the red and blue arrows. This can be understood by the fact that the electrons are driven by the optical field around respective valleys following the same reciprocal trajectories, including the same cycling direction. For electrons around the \mathbf{K} and \mathbf{K}' points, they accumulate dynamical phases similarly, but geometric phases and transition dipole phases oppositely, which lead to growing or canceling electron populations for different valleys in CB (45). As a result, the residual photocurrent dominantly originates from one valley only, thereby generating the valley-polarized currents. This process occurs in each optical cycle, allowing great potential for generating and modulating valley-polarized currents in sub-optical-cycle timescales.

It is worth noting that, according to the principle of our scheme, it primarily relies on the helical and asymmetric waveform of the optical field to initialize the valley-polarization and induce the currents, which are independent of the specific material properties. Thus, this scheme will apply to a

broad range of valley-active materials. In the following sections, we will demonstrate its feasibility through numerical simulations using the two most widely employed valley-active materials, gapped graphene and TMDs, respectively.

Valley-polarized currents in gapped graphene

Due to its unique electronic properties and high mobility, graphene has emerged as a promising material for valleytronic nanosystems (11, 16, 18, 20, 22–25, 46). In this section, we demonstrate the valley-polarized current manipulation in the gapped graphene with 0.4 eV gap. The electronic dynamics in the gapped graphene is described by solving the density matrix equations based on a tight-binding model (45, 47). Technical details are provided in the Methods.

Firstly, to verify the aforementioned idea of generating valley-polarized currents, we consider an example set of laser parameters with the fundamental wavelength of 5000 nm and the total intensity $I = I_1 + I_2 = 1 \times 10^9 \text{ W/cm}^2$. The relative phase θ is 0, and the intensity ratio I_2/I_1 is 1. The driving laser pulse is characterized by a sine-squared envelope with a full width at half maximum (FWHM) of 36.5 fs. A 35 fs decoherence time is used in this simulation.

Figure 2A illustrates the x and y components of the time-dependent vector potential of the driving field. Due to the helical waveform of the field, the electrons around the \mathbf{K} point are predominantly excited, as shown in Fig. 2B. Thus, the electron population around \mathbf{K} point (Fig. 2D) is significantly larger than that of \mathbf{K}' point (Fig. 2E). Furthermore, the electron population in CB is displaced along the negative k_y axis by the asymmetric A_y . Consequently, the intraband current along the negative y axis is generated, as shown in Fig. 2C. Here, the intraband current is calculated as:

$$\mathbf{J} = \mathbf{J}^{\mathbf{K}} + \mathbf{J}^{\mathbf{K}'} = \int_{\text{BZ1}} 2^2 N_c(\mathbf{k}) \frac{\partial E_c(\mathbf{k})}{\partial \mathbf{k}} d\mathbf{k} + \int_{\text{BZ2}} 2^2 N_c(\mathbf{k}) \frac{\partial E_c(\mathbf{k})}{\partial \mathbf{k}} d\mathbf{k}, \quad (3)$$

where the BZ1 (BZ2) represents the region around \mathbf{K} (\mathbf{K}'), as shown in Fig. 1C, E_c denotes energy of the CB, and $N_c(\mathbf{k})$ is the electron population on the CB.

Combined with the fact that there are more electrons excited in the vicinity of the \mathbf{K} point (see Fig. 2D and E), the total current \mathbf{J} dominantly originates from \mathbf{K} point (see the red and blue double arrows in Fig. 2C). Namely, a highly valley-polarized current is obtained. Its purity, evaluated by $\eta = (|\mathbf{J}^{\mathbf{K}}| - |\mathbf{J}^{\mathbf{K}'}|) / (|\mathbf{J}^{\mathbf{K}}| + |\mathbf{J}^{\mathbf{K}'}|)$, is $\eta = 68\%$. Besides, as shown by the solid red and blue lines in

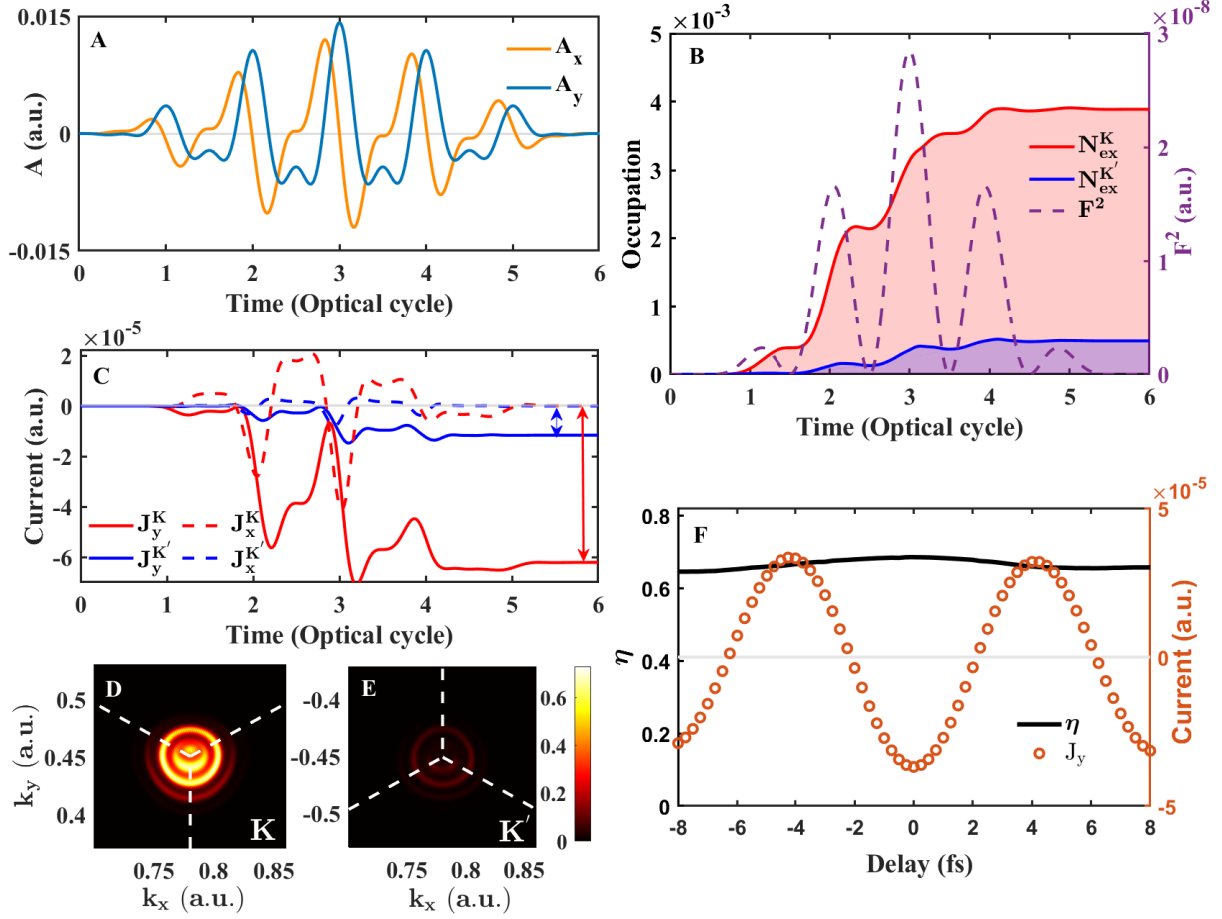


Fig. 2: Valley-polarized currents in gapped graphene. (A) The vector potential of the driving field. (B) The time evolution of electron occupation around two valleys in the CB and the square of the time-dependent electric field of the driving laser $F^2(t)$. (C) The x and y components of the currents from different valleys. (D)(E) The residual momentum-resolved electron population around \mathbf{K} and \mathbf{K}' in CB, respectively. (F) The dependence of the calculated J_y and corresponding η on the delay of the double-frequency component of the driving laser.

Fig. 2C, the valley-polarized current merges in one optical cycle. This indicates that our scheme also works for the shorter few-cycle laser pulses, and the valley-polarized currents can be manipulated on the sub-optical-cycle timescale.

In Fig. 2F, we demonstrate the sub-optical-cycle manipulation of valley-polarized currents. By delaying the double-frequency component, the driving optical field is tuned and the sub-cycle electron dynamics can be finely controlled (48, 49). Accordingly, the current along the y direction exhibits an oscillation with a period of 8 fs, signifying a pivotal advancement toward PHz valleytronics. Besides, the calculated η shows good robustness to the delay.

Having validated the basic concept, we will next explore strategies for optimizing the valley-polarized currents by altering the parameters of the driving field. In Fig. 3A, the fundamental wavelength dependence of the valley-polarized current generation is depicted. The optical parameters remain consistent with those in Fig. 2, except for the fundamental wavelength. Within the range of 1000 – 6000 nm, the current from \mathbf{K} point (the red line) is significantly larger than the current from \mathbf{K}' point (the blue line), which confirms the generality of the scheme over the laser wavelengths. Consequently, the calculated η , depicted by the black line, reaches the maximum value at 2600 nm and 5000 nm (dashed pink and light blue line). The calculated η is 67% and 68%, respectively.

By varying the intensity ratio I_2/I_1 of bicircular fields, one can achieve significant control over the electron dynamics (28, 36), making it possible to enhance the purity of the generated valley-polarized currents. The impact of intensity ratio I_2/I_1 on the valley-polarized current generation with the optimal fundamental wavelengths 5000 nm and 2600 nm is shown in Fig. 3B and C, respectively. In the limit of $I_2 = 0$, the vector potential $\mathbf{A}(t)$ is symmetric, thus the residual electron population is symmetric around \mathbf{K} point, resulting in the absence of residual current, as shown in Fig. 3D. With the increase of intensity ratio, the symmetry breaking of $\mathbf{A}(t)$ increases and finally decreases (for the cases $I_2/I_1 = 0$ and $I_2/I_1 = \infty$, $\mathbf{A}(t)$ is symmetric). Thus, the symmetry breaking of the electron population around each valley in the CB increases and then decreases. Besides, the residual electron population around each valley is almost unchanged for different intensity ratios (not shown). Eventually, the currents from the two valleys also increase and then decrease with the increase of intensity ratio, as the red and blue lines show in Fig. 3B and C. Regarding the purity η , it is highest for small I_2/I_1 (the left regions in Fig. 3B and C). However, the generated currents

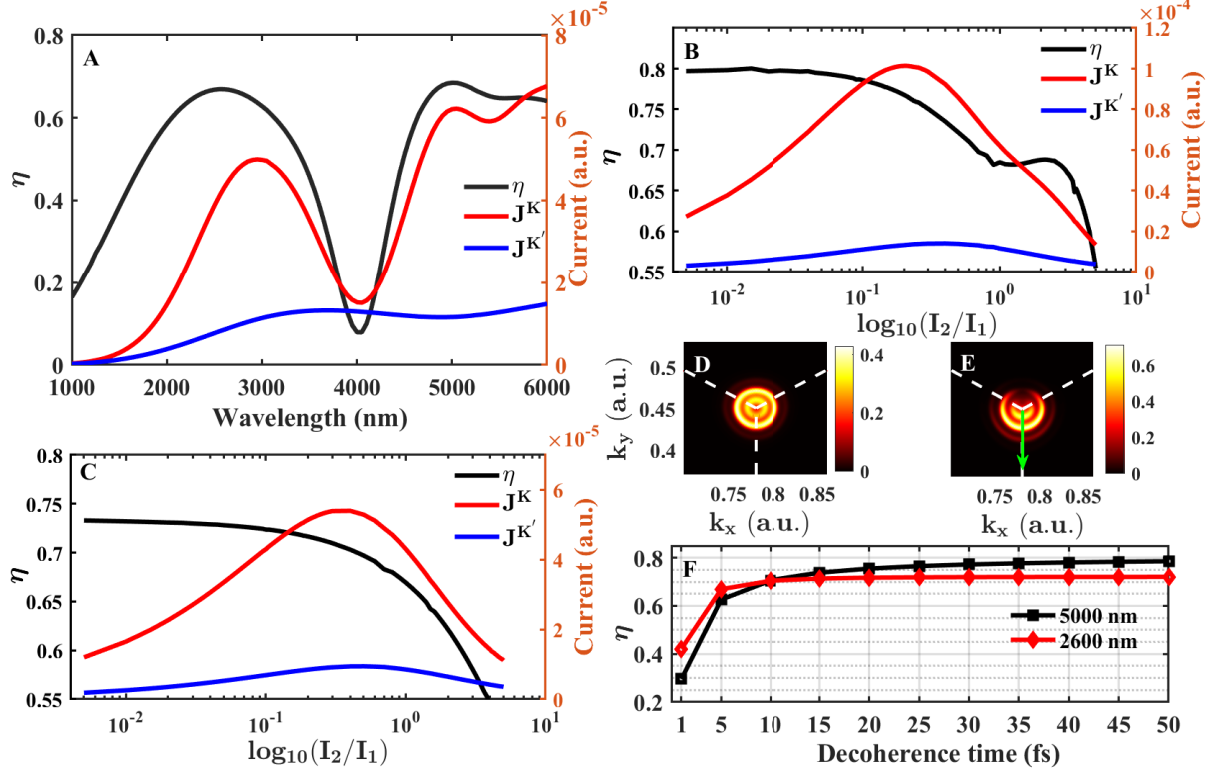


Fig. 3: (A) Fundamental wavelength dependence of the valley-polarized current generation. The optical parameters are the same as those for Fig. 2, except for the fundamental wavelength. (B)(C) Intensity ratio dependence of the valley-polarized current generation for the fundamental wavelength of 5000 nm and 2600 nm, respectively. (D)(E) The residual momentum-resolved electron population around \mathbf{K} point in CB with intensity ratio $I_2/I_1 = 0$ and 0.15, respectively. The corresponding fundamental wavelength is 5000 nm. The green arrows indicate the direction and magnitude of the valley-polarized currents. (F) Robustness of our scheme against decoherence considering the fundamental wavelength 5000 nm (black squares) and 2600 nm (red diamonds). The intensity ratio is $I_2/I_1 = 0.15$.

from the two valleys are both small in these cases, as the weak 2ω component causes only minimal symmetry breaking in the electron population around each valley. Thus, this configuration proves inadequate for the effective valley-polarized current generation. For the case of $I_2/I_1 = 0.15$, the purity of obtained valley-polarized current is 78% and 72% for 5000 nm and 2600 nm, respectively. Meanwhile, the generated currents are around their maximum values. This can be regarded as the optimal intensity ratio. The corresponding residual electron population around \mathbf{K} is shown in Fig. 3E, exhibiting a pronounced asymmetric distribution.

In Fig. 3F, the robustness of our scheme with respect to decoherence is demonstrated, where η is calculated with different decoherence times and the optimized laser parameters from Fig 3A to C ($I_2/I_1 = 0.15$ and fundamental wavelengths with 5000 nm and 2600 nm). For the case of 5000 nm (2600 nm), one can see that η decreases from 78% (72%) to 63% (67%), as the decoherence time reduces from 50 fs to 5 fs. Even for the extremely short decoherence time of 1 fs, it is still around 30% for 5000 nm (42% for 2600 nm). Therefore, our scheme is robust against the decoherence. This feature arises from the fact that the valley-polarized currents are established based on the ultrafast electron dynamics. Thus, our scheme is still suitable for materials with short decoherence time, like Weyl semimetals (a few femtoseconds, see (50–52)) and Dirac semimetals (for instance, around 10 fs for a typical 3D Dirac semimetal Cd_3As_2 (53, 54)).

Another advantage of the all-optical approach based on the tailored bichromatic optical field is the extremely high degree of freedom, allowing ultrafast manipulation of the valley-polarized currents. Finally, we demonstrate the precise modulation of the direction of valley-polarized current by adjusting the relative phase θ . According to the discussion based on Eq. 2, the symmetric axis of the electric field of the co-rotating bicircular field is oriented at $\mathbf{e}_{-\theta}$, along which the Lissajous figure is asymmetric. Likewise, one will find for the vector potential $\mathbf{A}(t) = -\int_{-\infty}^t \mathbf{F}(t')dt'$ that the symmetric axis is oriented at $\mathbf{e}_{-\theta+\pi/2}$, differing from that of the electric field by $\pi/2$. Consequently, it is expected that the residual electron population is displaced along $\mathbf{e}_{-\theta-\pi/2}$, which induces the residual valley-polarized current with the angle of $-\theta - \pi/2$, as shown by the solid black line in Fig. 4A.

To verify the above discussion, we numerically simulate the valley-polarized current generation with different relative phases. The directions of the resultant currents are depicted by the red stars in Fig. 4A. The optical parameters are the same as Fig. 2A, except for the relative phase θ . One can see

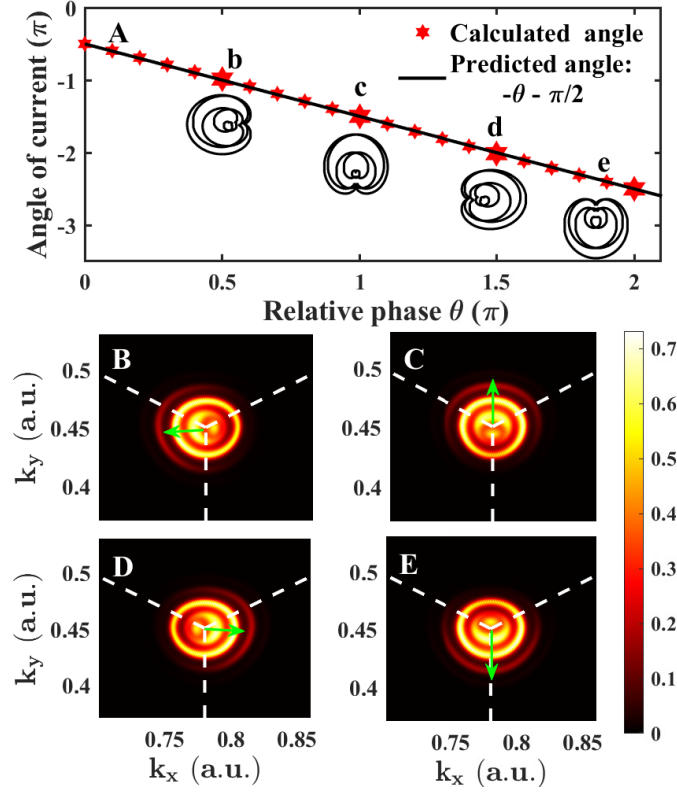


Fig. 4: (A) The red stars represent the direction of the calculated valley-polarized current with different relative phases θ . The solid black line indicates the predicted direction of the valley-polarized current. The inserts show the waveforms of co-rotating bicircular fields ($-\mathbf{A}(t)$) for $\theta = \pi/2, \pi, 3\pi/2,$ and 2π labeled by the big red stars b, c, d, and e, respectively. (B)-(E) The residual momentum-resolved electron population around \mathbf{K} point in CB for the relative phase $\theta = \pi/2, \pi, 3\pi/2,$ and 2π , corresponding to the big red stars b-e in (A). The green arrows indicate the direction and magnitude of the valley-polarized currents.

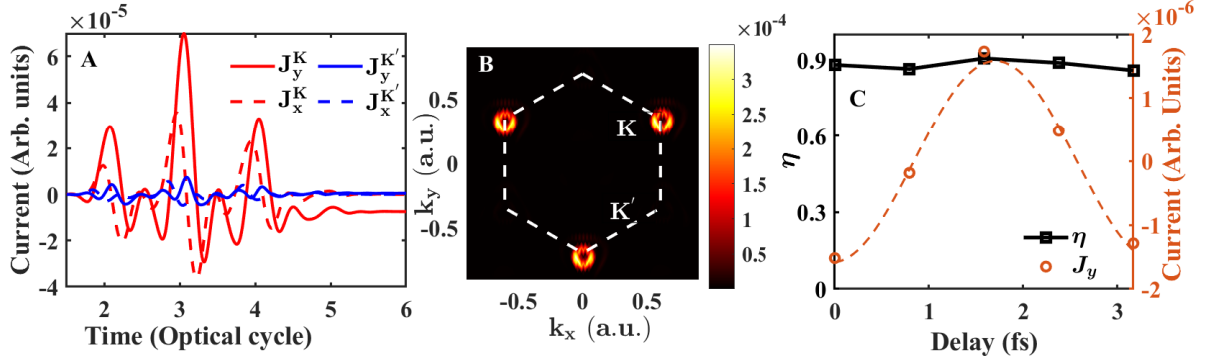


Fig. 5: Valley-polarized currents in MoS₂. (A) The x and y components of the currents from different valleys. (B) The residual momentum-resolved electron population in CB. (C) The dependence of the calculated J_y and corresponding η on the delay of the double-frequency component of the driving laser. The dashed orange line is drawn to guide the eye.

that the numerical results perfectly match the prediction. The corresponding residual momentum-resolved electron population around \mathbf{K} for four representative cases with $\theta = \pi/2, \pi, 3\pi/2$, and 2π are shown in Fig. 4B to E, respectively. Combined with the inserts in Fig. 4A, one can see that the displaced electron population varies with the orientation of the co-rotating bicircular fields, which reconfirms our theory.

The length of the green arrows in Fig. 4B to E indicates the magnitude of the corresponding residual currents, which remains nearly unchanged with the variation of θ . This feature allows ideal control over only the direction of valley-polarized currents without changing their magnitude.

Valley-polarized currents in MoS₂

Having demonstrated the fundamental physics and feasibility of our scheme with gapped graphene using a tight-binding model, we now examine its applicability to TMDs. The TMDs are the other promising class of material extensively explored for valleytronics. Compared with graphene, the TMDs have broader band gaps and stronger multielectron effects (55–57). Thus, the valley-polarized current generation in TMDs is studied using state-of-the-art TDDFT simulations. This method allows one to model the electron dynamics in solids without making strong assumptions and has been shown to provide good agreement between simulation results and experimental measurements (58, 59). The TDDFT simulations are performed with the real-space grid-based

code, Octopus (60–64). Technical details are provided in the Methods.

We take MoS₂ as a prototype. For the driving field, the fundamental wavelength is 1900 nm and the total intensity is 1×10^{11} W/cm². The FWHM of the laser pulse is 13.8 fs. The other optical parameters are consistent with those in Fig. 2A. The waveform of the driving field is similar to Fig. 2A, and A_y is still asymmetric. The result is shown in Fig. 5A. One can see that the magnitude of the current originating from the **K** point ($J_y^{\mathbf{K}}$) is much higher than that from the **K'** point ($J_y^{\mathbf{K}'}$). Thus, a significant valley-polarized current is obtained along the negative y direction with the purity of 88%. As previously discussed, the emergence of the nonvanishing current results from the displacement of the electron population due to the asymmetric driving field and the high purity results from the distinct excitation rates at different valleys (see Fig. 5B). We also calculate the current in MoS₂ by delaying the double-frequency component, as shown in Fig. 5C. Similarly, the current along the y direction oscillates with a period of 3.5 fs while η remains robust to the variation of the delay. These results suggest that our approach is model-independent, cross-validating its feasibility across a wide range of valley-active materials.

Discussion

In conclusion, we theoretically propose and demonstrate the first all-optical scheme for generating and modulating valley-polarized currents at optical frequencies. By applying non-resonant co-rotating bicircular driving fields, we achieve helical and asymmetric waveforms that concurrently induce valley-polarization and population displacement on the sub-optical-cycle timescale. This approach is primarily dependent on the effects of the waveform of the driving field and thus should apply to a broad range of valley-active materials. The feasibility is further supported by numerical simulations on the two typical categories of valley-active materials: gapped graphene and TMDs. The results also demonstrate that our scheme is robust against decoherence, with the purity only slightly decreasing even when the decoherence time falls to 5 fs. Note that, although multi-cycle optical pulses are employed in the numerical demonstration, our scheme also works for even shorter few-cycle pulses as the valley-polarized currents stem from the sub-cycle electron dynamics. In addition, the direction of the currents can be precisely controlled by adjusting the relative phase

of the bichromatic fields, with the magnitude of the current nearly unchanged. Our all-optical scheme represents a promising avenue for manipulating high-purity valley-polarized currents at the femtosecond timescale, opening the door to the new realm of PHz valleytronics.

Methods

Tight-binding simulation for gapped graphene

The electron dynamics in graphene under the laser fields is described as the time-dependent Schrödinger equation (TDSE):

$$i \frac{\partial \Psi}{\partial t} = H \Psi. \quad (4)$$

H is the Hamiltonian in the length gauge with a driving field $\mathbf{F}(t)$, with the following form:

$$H(\mathbf{r}, t) = H_0 + \mathbf{r} \cdot \mathbf{F}(t), \quad (5)$$

where H_0 is the field-free Hamiltonian of the target material. Atomic units are used unless otherwise stated. $\mathbf{F}(t) = f(t)\mathbf{F}_{\text{co}}(t)$. $f(t)$ is the envelope function of the laser pulse with a sine squared shape. In this work, the gapped graphene is described by a 2D two-band model with a tight-binding approximation. In this model, H_0 can be written as (65):

$$H_0 = \begin{pmatrix} \frac{\Delta}{2} & -\gamma f(\mathbf{k}) \\ -\gamma f^*(\mathbf{k}) & -\frac{\Delta}{2} \end{pmatrix}. \quad (6)$$

Here, Δ is the band gap between the valence band (VB) and the conduction band (CB), γ is the hopping parameter between nearest neighboring atoms and $f(\mathbf{k}) = \exp(i \frac{ak_x}{\sqrt{3}}) + 2 \exp(-i \frac{ak_x}{2\sqrt{3}}) \cos(\frac{k_y}{2})$, where a is the lattice constant of target materials. For the graphene, the lattice constant a and the hopping term γ are 0.246 nm and -3.03 eV, respectively. The band gap Δ is set to 0.4 eV.

The response of the laser-driven electron can be simulated by solving the 2D two-band density matrix equations (45, 47):

$$\begin{aligned} \dot{\Pi}(\mathbf{k}(t)) &= -\frac{\Pi(\mathbf{k}(t))}{T_2} + i\Omega^*(\mathbf{k}(t))\alpha(\mathbf{k}(t))e^{iS(\mathbf{k}(t))}, \\ \dot{n}_m(\mathbf{k}(t)) &= i s_m \Omega(\mathbf{k}(t))\Pi(\mathbf{k}(t))e^{-iS(\mathbf{k}(t))} + \text{c.c.}, \end{aligned} \quad (7)$$

where n_m is the the electron population of the VB ($m = v$) and the CB ($m = c$), Π is the off-diagonal element of the density matrix, and $\alpha = N_v - N_c$ is the population difference. $s_m = 1$ and -1 for $m = v$ and c , respectively. $\Omega = \mathbf{F} \cdot \mathbf{d}_{cv}$ is the Rabi frequency, where $\mathbf{d}_{cv} = \langle \Psi_{\mathbf{k}}^c | i \frac{\partial}{\partial \mathbf{k}} | \Psi_{\mathbf{k}}^v \rangle$ is the transition dipole. S is the accumulated phase during the evolution in the reciprocal space (45, 47). $\mathbf{k}(t) = \mathbf{k}_0 + \mathbf{A}(t)$, \mathbf{k}_0 is the initial wavenumber. T_2 is the decoherence time.

In the numerical simulation, we sample the first Brillouin zone using a grid with 901×901 points. The fourth-order Runge-Kutta method is used to solve the density matrix equations. The step size of the time grid is 0.1 a.u. The convergence of simulations has been tested.

TDDFT simulation for MoS₂

The electron dynamics in MoS₂ are simulated using the TDDFT. The evolution of the system is described by the time-dependent Kohn-Sham (KS) equations within the adiabatic approximation, represented in real space and the velocity gauge, given in atomic units by:

$$i\partial_t \varphi_{n,\mathbf{k}}^{\text{KS}}(t) = \left(\frac{1}{2} (-i\nabla + \mathbf{A}(t))^2 + v_{\text{KS}}(\mathbf{r}, t) \right) \varphi_{n,\mathbf{k}}^{\text{KS}}(t), \quad (8)$$

where $\varphi_{n,\mathbf{k}}^{\text{KS}}(t)$ is the KS-Bloch state at k-point \mathbf{k} and band index n and $v_{\text{KS}}(\mathbf{r}, t)$ is the time-dependent KS potential given by

$$v_{\text{KS}}(\mathbf{r}, t) = v_{\text{ion}}(\mathbf{r}, t) + v_H(\mathbf{r}, t) + v_{\text{xc}}(\mathbf{r}, t). \quad (9)$$

$v_{\text{ion}}(\mathbf{r}, t)$ represents the ionic potential. $v_H(\mathbf{r}, t)$ is the Hartree potential describing the classical electron-electron interaction. $v_{\text{xc}}(\mathbf{r}, t)$ is the exchange–correlation potential.

The structure of the monolayer MoS₂ is constructed by its primitive cell, using a real space spacing of 0.3 a.u. The lattice constant is 0.318 nm. The vertical separation between sulphur layers is 0.311 nm.

We added additional vacuum spacing above and below the monolayer MoS₂ of 33 a.u. in each direction of the non-periodic axis. Meanwhile, an absorbing region with a width of 3 a.u. is included to avoid spurious reflections. A Γ -centered $42 \times 42 \times 1$ k-grid is employed in the simulations. The KS wave functions are propagated with a time step of $\Delta t = 0.25$ a.u. Convergence has been tested for grid spacing, k-grid, and time step.

Calculations were performed using the local density approximation. The frozen core approx-

imation was used by the Optimized Norm-Conserving Vanderbilt Perdew-Burke-Ernzerhof pseudopotentials (66).

References and Notes

1. H. Yu, X. Cui, X. Xu, W. Yao, Valley excitons in two-dimensional semiconductors. *Natl. Sci. Rev.* **2** (1), 57–70 (2015), doi:10.1093/nsr/nwu078.
2. J. R. Schaibley, *et al.*, Valleytronics in 2D materials. *Nat. Rev. Mater.* **1** (11) (2016), doi:10.1038/natrevmats.2016.55.
3. S. A. Vitale, *et al.*, Valleytronics: opportunities, challenges, and paths forward. *Small* **14** (38), 1801483 (2018), doi:10.1002/sml.201801483.
4. D. Xiao, W. Yao, Q. Niu, Valley-contrasting physics in graphene: magnetic moment and topological transport. *Phys. Rev. Lett.* **99** (23), 236809 (2007), doi:10.1103/physrevlett.99.236809.
5. K. F. Mak, K. He, J. Shan, T. F. Heinz, Control of valley polarization in monolayer MoS₂ by optical helicity. *Nat. Nanotechnology* **7** (8), 494–498 (2012), doi:10.1038/nnano.2012.96.
6. D. Xiao, G.-B. Liu, W. Feng, X. Xu, W. Yao, Coupled spin and valley physics in monolayers of MoS₂ and other group-VI dichalcogenides. *Phys. Rev. Lett.* **108** (19), 196802 (2012), doi:10.1103/physrevlett.108.196802.
7. U. De Giovannini, H. Hübener, A. Rubio, Monitoring electron-photon dressing in WSe₂. *Nano Letters* **16** (12), 7993–7998 (2016), doi:10.1021/acs.nanolett.6b04419.
8. S. A. Oliaei Motlagh, J.-S. Wu, V. Apalkov, M. I. Stockman, Femtosecond valley polarization and topological resonances in transition metal dichalcogenides. *Phys. Rev. B* **98** (8), 081406 (2018), doi:10.1103/physrevb.98.081406.
9. Á. Jiménez-Galán., R. E. F. Silva, O. Smirnova, M. Ivanov, Lightwave control of topological properties in 2D materials for sub-cycle and non-resonant valley manipulation. *Nat. Photonics* **14** (12), 728–732 (2020), doi:10.1038/s41566-020-00717-3.

10. Á. Jiménez-Galán, R. E. F. Silva, O. Smirnova, M. Ivanov, Sub-cycle valleytronics: control of valley polarization using few-cycle linearly polarized pulses. *Optica* **8** (3), 277 (2021), doi:10.1364/optica.404257.
11. M. S. Mrudul, A. Jiménez-Galán, M. Ivanov, G. Dixit, Light-induced valleytronics in pristine graphene. *Optica* **8** (3), 422 (2021), doi:10.1364/optica.418152.
12. S. Sharma, P. Elliott, S. Shallcross, Valley control by linearly polarized laser pulses: example of WSe₂. *Optica* **9** (8), 947 (2022), doi:10.1364/optica.458991.
13. S. Sharma, J. K. Dewhurst, S. Shallcross, Light-shaping of valley states. *Nano Lett.* **23** (24), 11533–11539 (2023), doi:10.1021/acs.nanolett.3c03245.
14. I. Tyulnev, *et al.*, Valleytronics in bulk MoS₂ with a topologic optical field. *Nature* **628** (8009), 746–751 (2024), doi:10.1038/s41586-024-07156-y.
15. S. Mitra, *et al.*, Light-wave-controlled Haldane model in monolayer hexagonal boron nitride. *Nature* **628** (8009), 752–757 (2024), doi:10.1038/s41586-024-07244-z.
16. A. Rycerz, J. Tworzydło, C. W. J. Beenakker, Valley filter and valley valve in graphene. *Nat. Phys.* **3** (3), 172–175 (2007), doi:10.1038/nphys547.
17. L. Zhang, *et al.*, Generation and transport of valley-polarized current in transition-metal dichalcogenides. *Phys. Rev. B* **90** (19), 195428 (2014), doi:10.1103/physrevb.90.195428.
18. R. V. Gorbachev, *et al.*, Detecting topological currents in graphene superlattices. *Science* **346** (6208), 448–451 (2014), doi:10.1126/science.1254966.
19. K. F. Mak, K. L. McGill, J. Park, P. L. McEuen, The valley Hall effect in MoS₂ transistors. *Science* **344** (6191), 1489–1492 (2014), doi:10.1126/science.1250140.
20. Y. Shimazaki, *et al.*, Generation and detection of pure valley current by electrically induced Berry curvature in bilayer graphene. *Nat. Phys.* **11** (12), 1032–1036 (2015), doi:10.1038/nphys3551.
21. C. Jin, *et al.*, Imaging of pure spin-valley diffusion current in WS₂-WSe₂ heterostructures. *Science* **360** (6391), 893–896 (2018), doi:10.1126/science.aao3503.

22. Y. Jiang, T. Low, K. Chang, M. I. Katsnelson, F. Guinea, Generation of pure bulk valley current in graphene. *Phys. Rev. Lett.* **110** (4), 046601 (2013), doi:10.1103/physrevlett.110.046601.
23. M. Settnes, S. R. Power, M. Brandbyge, A.-P. Jauho, Graphene nanobubbles as valley filters and beam splitters. *Phys. Rev. Lett.* **117** (27), 276801 (2016), doi:10.1103/physrevlett.117.276801.
24. R. Gupta, F. Rost, M. Fleischmann, S. Sharma, S. Shallcross, Straintronics beyond homogeneous deformation. *Phys. Rev. B* **99** (12), 125407 (2019), doi:10.1103/physrevb.99.125407.
25. C.-C. Hsu, M. L. Teague, J.-Q. Wang, N.-C. Yeh, Nanoscale strain engineering of giant pseudo-magnetic fields, valley polarization, and topological channels in graphene. *Sci. Adv.* **6** (19), eaat9488 (2020), doi:10.1126/sciadv.aat9488.
26. S. Sharma, P. Elliott, S. Shallcross, THz induced giant spin and valley currents. *Sci. Adv.* **9** (11), eadf3673 (2023), doi:10.1126/sciadv.adf3673.
27. S. Sharma, D. Gill, S. Shallcross, Giant and controllable valley currents in graphene by double pumped THz light. *Nano Lett.* **23** (22), 10305–10310 (2023), doi:10.1021/acs.nanolett.3c02874.
28. D. B. Milošević, W. Becker, R. Kopold, Generation of circularly polarized high-order harmonics by two-color coplanar field mixing. *Phys. Rev. A* **61** (6), 063403 (2000), doi:10.1103/physreva.61.063403.
29. A. Fleischer, O. Kfir, T. Diskin, P. Sidorenko, O. Cohen, Spin angular momentum and tunable polarization in high-harmonic generation. *Nat. Photonics* **8** (7), 543–549 (2014), doi:10.1038/nphoton.2014.108.
30. O. Kfir, *et al.*, Generation of bright phase-matched circularly-polarized extreme ultraviolet high harmonics. *Nat. Photonics* **9** (2), 99–105 (2014), doi:10.1038/nphoton.2014.293.
31. D. M. Reich, L. B. Madsen, Illuminating molecular symmetries with bicircular high-order-harmonic generation. *Phys. Rev. Lett.* **117** (13), 133902 (2016), doi:10.1103/physrevlett.117.133902.

32. M. Han, P. Ge, Y. Shao, Q. Gong, Y. Liu, Attoclock photoelectron interferometry with two-color corotating circular fields to probe the phase and the amplitude of emitting wave packets. *Phys. Rev. Lett.* **120** (7), 073202 (2018), doi:10.1103/physrevlett.120.073202.
33. T. Heinrich, *et al.*, Chiral high-harmonic generation and spectroscopy on solid surfaces using polarization-tailored strong fields. *Nat Commun* **12** (1) (2021), doi:10.1038/s41467-021-23999-9.
34. O. Neufeld, N. Tancogne-Dejean, U. De Giovannini, H. Hübener, A. Rubio, Light-driven extremely nonlinear bulk photogalvanic currents. *Phys. Rev. Lett.* **127** (12), 126601 (2021), doi:10.1103/physrevlett.127.126601.
35. W. Li, X. Zhu, P. Lan, P. Lu, Elliptically polarized attosecond pulse generation by corotating bicircular laser fields. *Phys. Rev. A* **106** (4), 043115 (2022), doi:10.1103/physreva.106.043115.
36. X. Zhu, P. Lu, M. Lein, Control of the Geometric Phase and Nonequivalence between Geometric-Phase Definitions in the Adiabatic Limit. *Phys. Rev. Lett.* **128** (3), 030401 (2022), doi:10.1103/physrevlett.128.030401.
37. M. Tani, K. Sasaki, Y. Shinohara, K. L. Ishikawa, Enhanced energy deposition and carrier generation in silicon induced by two-color intense femtosecond laser pulses. *Phys. Rev. B* **106** (19), 195141 (2022), doi:10.1103/physrevb.106.195141.
38. G. Lerner, *et al.*, Multiscale dynamical symmetries and selection rules in nonlinear optics. *Science Advances* **9** (15), eade0953 (2023), doi:10.1126/sciadv.ade0953.
39. A. Wirth, *et al.*, Synthesized Light Transients. *Science* **334** (6053), 195–200 (2011), doi:10.1126/science.1210268.
40. P. Ge, M. Han, Y. Deng, Q. Gong, Y. Liu, Universal description of the attoclock with two-color corotating circular fields. *Phys. Rev. Lett.* **122** (1), 013201 (2019), doi:10.1103/physrevlett.122.013201.
41. I. Babushkin, *et al.*, All-optical attoclock for imaging tunnelling wavepackets. *Nat. Phys.* **18** (4), 417–422 (2022), doi:10.1038/s41567-022-01505-2.

42. D. M. Reich, L. B. Madsen, Rotating-frame perspective on high-order-harmonic generation of circularly polarized light. *Phys. Rev. A* **93** (4), 043411 (2016), doi:10.1103/physreva.93.043411.
43. L. Li, *et al.*, Reciprocal-space-trajectory perspective on high-harmonic generation in solids. *Phys. Rev. Lett.* **122** (19), 193901 (2019), doi:10.1103/physrevlett.122.193901.
44. N. Sun, X. Zhu, L. Li, P. Lan, P. Lu, Cutoff extension of high harmonics via resonant electron injection channels. *Phys. Rev. A* **103** (5), 053111 (2021), doi:10.1103/physreva.103.053111.
45. H. Cui, *et al.*, Valley-resolved interband excitation and emission in gapped graphene. *Phys. Rev. A* **106** (4), 043505 (2022), doi:10.1103/physreva.106.043505.
46. K. L. Ishikawa, Nonlinear optical response of graphene in time domain. *Physical Review B* **82** (20), 201402 (2010), doi:10.1103/physrevb.82.201402.
47. G. Vampa, *et al.*, Theoretical analysis of high-harmonic generation in solids. *Phys. Rev. Lett.* **113** (7), 073901 (2014), doi:10.1103/physrevlett.113.073901.
48. A. Schiffrin, *et al.*, Optical-field-induced current in dielectrics. *Nature* **493** (7430), 70–74 (2012), doi:10.1038/nature11567.
49. M. Guan, S. Hu, H. Zhao, C. Lian, S. Meng, Toward attosecond control of electron dynamics in two-dimensional materials. *Applied Physics Letters* **116** (4) (2020), doi:10.1063/1.5135599.
50. A. Bharti, M. S. Mrudul, G. Dixit, High-harmonic spectroscopy of light-driven nonlinear anisotropic anomalous Hall effect in a Weyl semimetal. *Phys. Rev. B* **105** (15), 155140 (2022), doi:10.1103/physrevb.105.155140.
51. L. Medic, J. Mravlje, A. Ramšak, T. Rejec, High-harmonic generation in semi-Dirac and Weyl semimetals with broken time-reversal symmetry: Exploration of the merging of Weyl nodes. *Phys. Rev. B* **109** (20), 205130 (2024), doi:10.1103/physrevb.109.205130.
52. H. Hübener, M. A. Sentef, U. De Giovannini, A. F. Kemper, A. Rubio, Creating stable Floquet–Weyl semimetals by laser-driving of 3D Dirac materials. *Nature Communications* **8** (1) (2017), doi:10.1038/ncomms13940.

53. S. Kovalev, *et al.*, Non-perturbative terahertz high-harmonic generation in the three-dimensional Dirac semimetal Cd_3As_2 . *Nat Commun* **11** (1) (2020), doi:10.1038/s41467-020-16133-8.
54. S. Germanskiy, *et al.*, Ellipticity control of terahertz high-harmonic generation in a Dirac semimetal. *Phys. Rev. B* **106** (8), 1081127 (2022), doi:10.1103/physrevb.106.1081127.
55. H. Liu, *et al.*, High-harmonic generation from an atomically thin semiconductor. *Nat. Phys.* **13** (3), 262–265 (2016), doi:10.1038/nphys3946.
56. I. Tikhomirov, T. Sato, K. L. Ishikawa, High-harmonic generation enhanced by dynamical electron correlation. *Phys. Rev. Lett.* **118** (20), 203202 (2017), doi:10.1103/physrevlett.118.203202.
57. V. Chang Lee, L. Yue, M. B. Gaarde, Y.-h. Chan, D. Y. Qiu, Many-body enhancement of high-harmonic generation in monolayer MoS_2 . *Nat Commun* **15** (1) (2024), doi:10.1038/s41467-024-50534-3.
58. N. Klemke, *et al.*, Polarization-state-resolved high-harmonic spectroscopy of solids. *Nat Commun* **10** (1) (2019), doi:10.1038/s41467-019-09328-1.
59. Z. Schumacher, *et al.*, Ultrafast electron localization and screening in a transition metal dichalcogenide. *Proc. Natl. Acad. Sci.* **120** (15) (2023), doi:10.1073/pnas.2221725120.
60. M. Marques, octopus: a first-principles tool for excited electron–ion dynamics. *Comput. Phys. Commun.* **151** (1), 60–78 (2003), doi:10.1016/s0010-4655(02)00686-0.
61. A. Castro, *et al.*, octopus: a tool for the application of time-dependent density functional theory. *Phys. Status Solidi B* **243** (11), 2465–2488 (2006), doi:10.1002/pssb.200642067.
62. X. Andrade, *et al.*, Real-space grids and the Octopus code as tools for the development of new simulation approaches for electronic systems. *Phys. Chem. Chem. Phys.* **17** (47), 31371–31396 (2015), doi:10.1039/c5cp00351b.
63. H. Hübener, U. De Giovannini, A. Rubio, Phonon Driven Floquet Matter. *Nano Letters* **18** (2), 1535–1542 (2018), doi:10.1021/acs.nanolett.7b05391.

64. N. Tancogne-Dejean, *et al.*, Octopus, a computational framework for exploring light-driven phenomena and quantum dynamics in extended and finite systems. *J. Chem. Phys.* **152** (12) (2020), doi:10.1063/1.5142502.
65. T. G. Pedersen, A.-P. Jauho, K. Pedersen, Optical response and excitons in gapped graphene. *Phys. Rev. B* **79** (11), 113406 (2009), doi:10.1103/physrevb.79.113406.
66. M. Schlipf, F. Gygi, Optimization algorithm for the generation of ONCV pseudopotentials. *Comput. Phys. Commun.* **196**, 36–44 (2015), doi:10.1016/j.cpc.2015.05.011.

Acknowledgement

The computation is completed in the HPC Platform of Huazhong University of Science and Technology. **Funding:** This work was supported by National Key Research and Development Program (Grant No. 2023YFA1406800 and No. 2022YFA1604403) and the National Natural Science Foundation of China (NSFC) (Grant Nos. 12174134, 12104172, 12021004 and 12374317). **Author contributions:** X. Z. conceived the ideas and coordinated the research project. W. L. performed the calculations and main analysis. All authors contributed to the discussion of the results and writing of the manuscript. **Competing interests:** The authors declare that they have no competing interests. **Data and materials availability:** All data needed to evaluate the conclusions in the paper are present in the paper. Additional data related to this paper may be requested from the authors.